ADVANCED FUNCTIONAL MATERIALS

FULL PAPER

DOI: 10.1002/adfm.200600499

Systematic Study of the Growth of Aligned Arrays of α-Fe_2O_3 and Fe_3O_4 Nanowires by a Vapor–Solid Process**

By *Yu-Lun Chueh*, *Ming-Wei Lai*, *Jia-Qi Liang*, *Li-Jen Chou*,* and *Zhong Lin Wang**

Growth of aligned and uniform α-Fe_2O_3 nanowire (NW) arrays has been achieved by a vapor–solid process. The experimental conditions, such as type of substrate, local growth and geometrical environment, gas-flow rate, and growth temperature, under which the high density α-Fe_2O_3 NW arrays can be grown by a vapor–solid route via the tip-growth mechanism have been systematically investigated. The density of the α-Fe_2O_3 NWs can be enhanced by increasing the concentration of Ni atoms inside the alloy substrate. The synthesized temperature can be as low as 400 °C. Fe_3O_4 NWs can be produced by converting α-Fe_2O_3 NWs in a reducing atmosphere at 450 °C. The transformation of phase and structure have been observed by in situ transmission electron microscopy. The magnetic and field-emission properties of the NWs indicate their potential applications in nanodevices.

1. Introduction

Nanowires (NWs) with different physical properties and structure characteristics can be used for a wide range of applications. Metallic NWs are applicable as interconnects for nanodevices, semiconductor NWs can be used to fabricate transistors and electro-optical devices,[1–5] and magnetic 1D nanomaterials have received much attention because of their potential applications in perpendicular data recording and spintronic devices.[6,7] Among magnetic materials, iron oxides, such as α-Fe_2O_3 and Fe_3O_4, are the most popular materials and possess many advantages in technological applications. In hexagonal or cubic close-packed structures, Fe ions partially fill in the octahedral or tetrahedral coordination.[8–11] α-Fe_2O_3 is an n-type semiconductor with a small bandgap of 2.1 eV. The crystal structure of α-Fe_2O_3 is identical to that of corundum (space group = $R3c$) and can be described as a hexagonal close-packed system with oxygen ions stacked along the [001] direction. Namely, planes of anions are parallel to the (001) planes (it can also be an index in a rhombohedral system), with lattice constants of α-Fe_2O_3 of $a_0 = 0.5034$ nm and $c_0 = 1.375$ nm.[12] So far, NWs of α-Fe_2O_3 have been synthesized by several groups using solid-phase reactions by oxidizing bulk iron in a mixed-gas ambient containing CO_2, O_2, N_2, SO_2, H_2O, etc. in temperature ranges of 600–700 °C.[13,14] Fe_3O_4, on the other hand, has an inverse spinel structure with a face-centered cubic unit cell of 32 O^{2-} ions with a lattice constant of 0.839 nm, in which one third of the iron ions occupy the tetrahedral sites (all Fe^{3+}), while two thirds of the iron ions occupy both the octahedral and tetrahedral sites (one half is Fe^{2+} and the other half is Fe^{3+}).[12] The synthesis of Fe_3O_4 nanomaterials normally occurs via a chemical route, which is based on the hydrothermal process,[15,16] and only a few reports are available about the synthesis of Fe_3O_4 NWs using a vapor-phase route.[17–19]

For the other oxide nanowires, such as ZnO, MgO, and In_2O_3, the growth phenomena have been systematically investigated using various growth parameters.[20–22] Although α-Fe_2O_3 NWs have been successfully synthesized via the vapor–solid route, a systematic investigation of different parameters is still unavailable. In the present study, we have systematically investigated the various experimental conditions under which optimal NWs can be synthesized, including substrate position and orientation, the flow rate of the carrier gas, synthesis temperature, and growth substrate. Fe_3O_4 NWs have been formed by converting α-Fe_2O_3 NWs in a reductive ambient. The magnetic and field-emission properties of these NWs have been characterized.

2. Results and Discussion

The experimental procedures used during the vapor-phase growth are introduced in the Experimental section. Here we focus on a systematic investigation of the effect of the experi-

[*] Prof. L. J. Chou, Y. L. Chueh, M. W. Lai,[+] J. Q. Liang
Department of Materials Science and Engineering
National Tsing Hua University
Hsinchu, Taiwan 300 (ROC)
E-mail: ljchou@mx.nthu.edu.tw
Prof. Z. L. Wang, Y. L. Chueh
School of Materials Science and Engineering
Georgia Institute of Technology
Atlanta, GA 30332-0245 (USA)
E-mail: zhong.wang@mse.gatech.edu
[+] Present address: Industrial Technology Research Institute, Tainan, Taiwan, ROC.

[**] This research was supported by the National Science Council through Grant No. NSC 94-2215-E-007-019, the Ministry of Education through Grant No. 93-E-FA04-1-4, the Thousand Horse Program No. 095-2917-1-007-014, NSF, the NASA Vehicle System Program, Department of Defense Research and Engineering (DDR&E), the Defense Advanced Research Project Agency (N66001-040-1-18903). Supporting information is available online from Wiley InterScience or from the author.

mental conditions and environment on the growth morphology and quality of the samples.

2.1. Effect of Alloyed Substrates on the Synthesis of α-Fe_2O_3 NWs

The first condition to be changed was the substrate used for the growth. Figure 1a–d shows the morphologies of NWs taken from the central areas of substrates consisting of different alloys, including $Fe_{0.5}Ni_{0.5}$, $Fe_{0.64}Ni_{0.36}$, Fe foil, and Fe film. The substrates were placed standing vertically on an alumina stage so that the vapor flowed directly against the surface of the substrate. The growth was conducted at 400 °C for 10 h in an Ar ambient at a vapor-flow rate of 100 sccm. It was found that the density of NWs significantly increased on increasing the Ni concentration in the alloy substrates. According to previous reports, the growth mechanism of the α-Fe_2O_3 NWs is quite different from that of other 1D nanomaterials, characterized by several important characteristics: the growth of micro-/nanostructures from the alloy substrate with a taperlike feature, the lengthening of the diameter at high temperatures, and the long growth time.[23] This well-known growth mechanism is called the tip-growth mechanism (proposed by Takagi), in which the surface defects inside the iron substrate play an important role in lowering the energy barrier, to serve as the nucleation sites for NW growth.[24] In addition, the surface defects can display various forms, such as linear and planar defects, resulting in different morphologies of Fe_2O_3 nanostructures under different growth conditions.[14] During the growth of one-dimensional iron oxide nanostructures, several iron oxide layers with thicknesses of several micrometers are subsequently formed before the growth of the NWs. These iron oxide layers, including those of FeO, Fe_xO ($x > 1$), Fe_3O_4, and Fe_2O_3, are formed below the surface of the alloy substrate and can serve as the reactants for interdiffusion after growth at high temperature, so that the iron atoms can constantly diffuse to the surface and form nucleation sites for growth of Fe_2O_3 NWs. Thus, growth of the NWs is mainly dominated by surface diffusion and internal diffusion.[24]

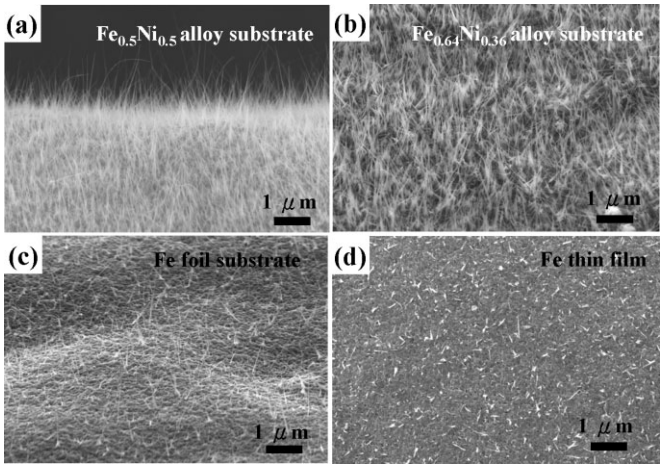

Figure 1. Scanning electron microscopy (SEM) images of α-Fe_2O_3 NWs synthesized on a) an $Fe_{0.5}Ni_{0.5}$ alloy substrate; b) an $Fe_{0.64}Ni_{0.36}$ alloy substrate; c) Fe foil; d) an Fe film evaporated by electron-beam deposition at 400 °C for 10 h in Ar ambient at 100 sccm.

The thickness of the iron film deposited on the Si substrate is only 1–2 μm, and most of the iron film is oxidized during the growth process, resulting in insufficient iron atoms from the substrate for NW growth. This is why the density of NWs on iron films deposited on Si substrates is significantly decreased (Fig. 1d). In addition, an increase in the concentration of Ni atoms in the Fe-based alloy can enhance the self-diffusion of Fe atoms inside the alloy substrate, resulting in an increased density of NWs.[25–27] The only carrier gas used in the present study is Ar. However, it can be considered that oxygen vapor is formed from the decomposition of α-Fe_2O_3 powder at 1200 °C (see Supporting Information).

2.2. Dependence of α-Fe_2O_3 NW Growth Morphology on the Local Substrate Environment

The local environment at the substrate can critically affect the growth morphology of the nanostructures. In the tube furnace, we first chose a vertically positioned substrate so that the local temperature across the entire substrate would be constant. The local "turbulence" or flow speed and pressure of the vapor phase and carrier gas could be investigated, as shown schematically in Figure 2a. Although the gas flow was stable and uniform in the entire tube furnace, the local variation could be significant. We chose four regions from bottom to top

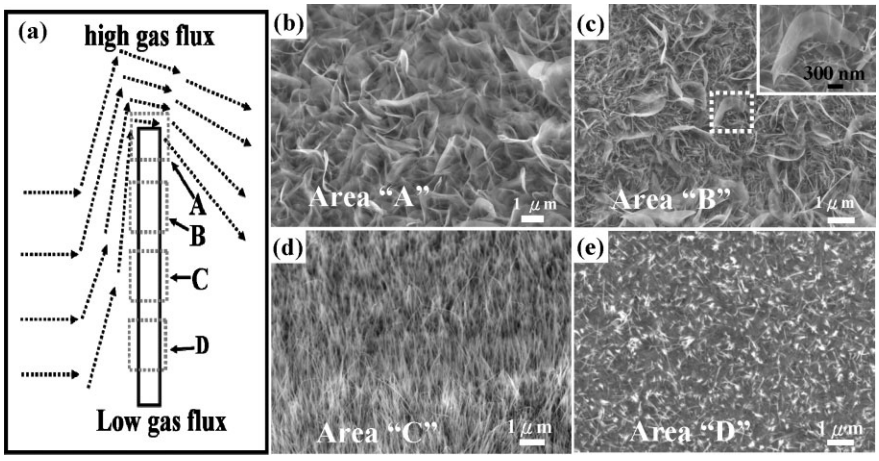

Figure 2. a) Schematic illustration of gas flux around the substrate that is placed vertically on an alumina stage. The different areas are marked as A–D. The corresponding SEM images are shown, respectively, in (b–e) for $Fe_{0.64}Ni_{0.36}$ samples after annealing at 400 °C for 10 h in Ar ambient at a flow rate of 100 sccm.

ADVANCED FUNCTIONAL MATERIALS

(labeled A to D) for the following study, and the corresponding structures grown on the $Fe_{64}Ni_{36}$ substrate at 400 °C for 10 h in an Ar ambient at a flow rate of 100 sccm are presented in Figure 2b–e. It is obvious that different morphologies were formed in the bottom and top regions. In region A, the morphology was sheetlike, and became a combination of sheetlike and NW-like in region B (Fig. 2b and c). The inset in Figure 2c shows a magnified scanning electron microscopy (SEM) image of the sheetlike feature. A wirelike morphology of uniform high density could be found in region C (Fig. 2d), while the density of NWs was significantly decreased in region D. A possible explanation can be attributed to the different concentrations of oxygen vapor in the local regions. The high flux provides a high concentration of oxygen vapor, resulting in an increased growth rate of the 2D structures.[14,28]

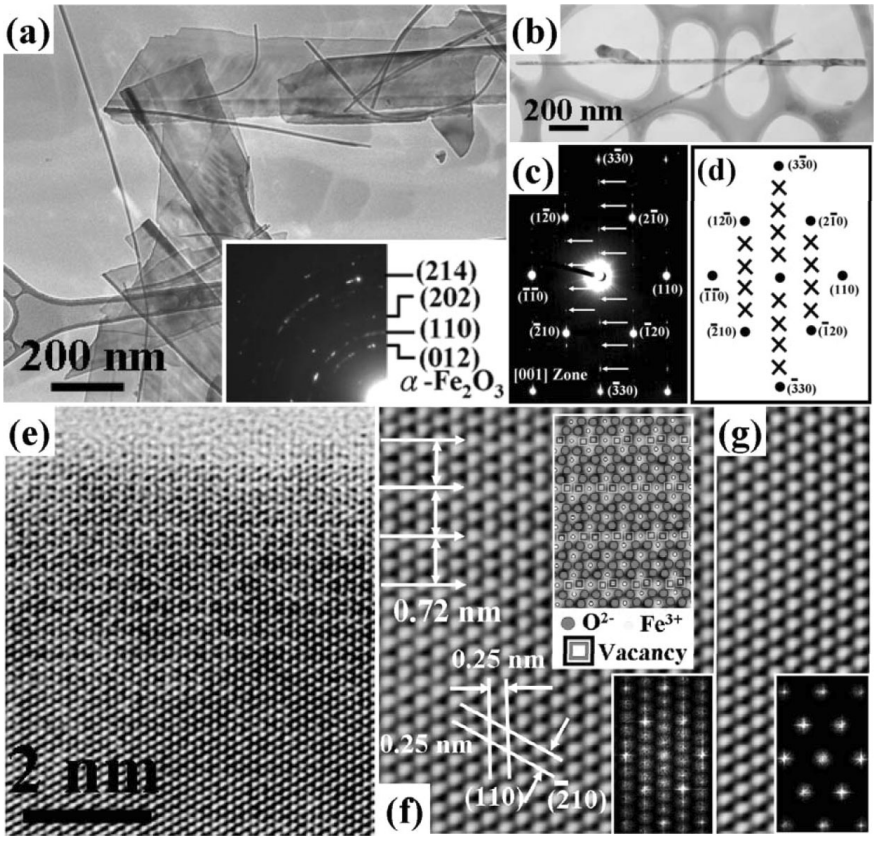

Figure 3. a,b) TEM images taken from the regions B and C shown in Figure 2a for the sample grown on $Fe_{0.64}Ni_{0.36}$ at 400 °C for 10 h in Ar ambient at a flow rate of 100 sccm. Inset in (a) shows the corresponding diffraction pattern. c) The diffraction pattern with [001] zone axis extracted from (b). The extra spots with five times $(3\bar{3}0)$ can be clearly found and are illustrated in (d). e) The high-resolution TEM image recorded from (b). It is clear that regular lines can be observed. f) The corresponding high-resolution TEM image. The hard-ball model fits the relative atomic position. The inset shows the fast-Fourier transform (FFT), which is consistent with the diffraction pattern in (c). g) The Fourier-filtered image formed by removing the extra reflection spots. The inset shows the corresponding FFT image without the extra spots.

2.3. Microstructure and Electron Energy-Loss Spectroscopy Analysis of the Samples

In order to understand the detailed structures of these nanomaterials, transmission electron microscopy (TEM) and electron energy-loss spectroscopy (EELS) were used. Figure 3a shows a TEM image taken from region B in Figure 2a. The corresponding diffraction pattern is shown in the inset of Figure 3a, where the individual planes are indexed, clearly revealing that the NW phase is α-Fe_2O_3. Figure 3b shows a low-magnification TEM image of the α-Fe_2O_3 NWs with diameters of 10–20 nm taken from region C. The corresponding diffraction pattern, as shown in the inset of Figure 3c, also confirms the α-Fe_2O_3 phase with a [001] zone axis. It is interesting that extra spots can be found in the diffraction pattern with $d = 1/5(3\bar{3}0)$, which has five times the distance of the $(3\bar{3}0)$ plane, as shown by arrow heads on detailed examination of the diffraction pattern, presented schematically in Figure 3d. Figure 3e shows a corresponding high-resolution TEM image that highlights the ordering feature. This superstructure is suggested to be caused by oxygen vacancies inside the α-Fe_2O_3 NWs during growth. Similar results were also found in previous reports and other materials.[24,29–31] The magnified high-resolution TEM image is shown in Figure 3f to explain the superstructure caused by the oxygen deficiencies. The two almost identical *d*-spacings of 0.25 nm are consistent with the *d*-values of $(2\bar{1}0)$ and (110), indicating the single-crystal feature with a growth direction along [110]. The long-range ordering phenomena with a period of 0.72 nm are located and marked by white arrow heads. The inset in the bottom of Figure 3f shows the corresponding fast Fourier transform (FFT) image, which is consistent with the results of the diffraction pattern. In order to clarify the ordering phenomenon found in both the diffraction pattern and FFT pattern from the high-resolution TEM image, respectively, the ideal high-resolution TEM image was processed by inverse FFT via selecting only the matrix reflections from the ideal α-Fe_2O_3 structure, and the result is shown in Figure 3g. On comparing the two high-resolution TEM images (Fig. 3f and g), the ambiguous lattice image along the white arrow heads between the two nearest bright dots can be found, which is suggested to be caused by ordered oxygen vacancies. Furthermore, the hard-ball model, formed by removing the oxygen atoms along the five period distances of the Fe–O lattice plane, fits coherently with the individual sites of the corresponding high-resolution TEM image, as shown in the middle inset of Figure 3f, where the dark-grey and light-grey balls and the double rectangle represent the oxygen anion, iron cation, and oxygen vacancies caused by the oxygen deficiency, respectively.

From the electronic structure, the presence of oxygen vacancies inside the α-Fe_2O_3 NWs could accompany a change in the

oxidation states of the nearest-neighbor Fe cations, which has been revealed by EELS at nanometer spatial resolution.[32] All of the raw data acquired by EELS have been calibrated on an energy scale by the zero-loss peak and deconvoluted by the low-loss region to reduce the multiple-scattering effect. Figure 4a shows the EELS spectrum of oxygen K-edge energy-loss near-edge fine structure (ELNES) for α-Fe_2O_3 NWs and commercial α-Fe_2O_3 powder. Four peaks, labeled a to d, can be found in the NW spectrum and the standard powder samples. In general, peak a is derived from the O 1s to 2p core level hybridized with the Fe 3d orbital, while peak b originates from

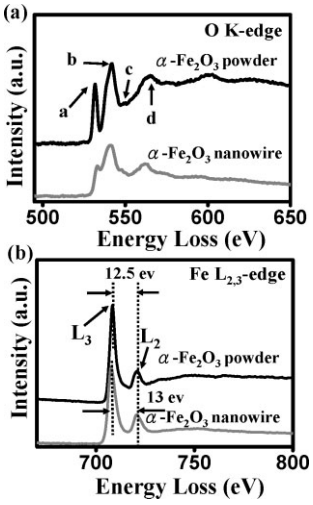

Figure 4. EELS spectrum of a) oxygen K-edge ELNES and b) Fe L-edge of α-Fe_2O_3 NWs and that of the standard sample.

the O 2p states hybridized with the transition metal 4s and 4p states.[33] The peaks c and d result from the scattering of the third and the first oxygen coordination shells by outgoing or backscattering electrons.[33,34] It is obvious that the intensities of peaks a and b for the NWs are less than those for the standard powder sample. The decreased intensity in peaks a and b is thought to be caused by oxygen vacancies inside α-Fe_2O_3 NWs, resulting in a diminishing hybridization of metal 3d orbitals with O 2p orbitals.[34] Similar results can be found for other materials such as γ-Fe_2O_3[35] and Ni-$BaTiO_3$.[29] In addition, the L edge can provide us with the ionization status of metal cations by determining the relative position and intensity of individual L_3 and L_2 edges, respectively.[36,37] The corresponding Fe $L_{2,3}$ edge spectra for commercial α-Fe_2O_3 powder and NW samples are shown in Figure 4b, where the L_3 and L_2 lines are the transitions $2p^{3/2} \rightarrow 3d^{3/2}3d^{5/2}$ and $2p^{1/2} \rightarrow 3d^{3/2}$, respectively.[31] The L_3 line is located at 708.9 eV for α-Fe_2O_3 powder and is separated by 12.5 eV from the L_2 line, while for α-Fe_2O_3 NWs, the L_3 line is located at 708.4 eV and is separated by 13 eV from the L_2 line. The chemical shift of 0.5 for the L_3 lines likely results from oxygen vacancies, which partially decrease the oxidation states of Fe cations from Fe^{3+} to Fe^{2+}.[33] In addition, the intensity ratio $I(L_3)/I(L_2)$ has been shown to be sensitive to the valance states of the transition metal oxide.[33] As a result, the intensity ratio $I(L_3)/I(L_2)$ for standard α-Fe_2O_3 powder is about 5.0, but this value is 4.2 for α-Fe_2O_3 NWs. The significant decrease in the intensity ratio confirms a change in the partial oxidation states of Fe^{3+} to Fe^{2+} and is consistent with other reports about the change in the oxidation states resulting from the oxygen vacancies in order to maintain the charge balance inside the α-Fe_2O_3 NWs.[33,35]

No Ni atoms can be found inside the α-Fe_2O_3 NWs when Fe–Ni alloy was used as the substrate. From existing studies about the oxidation of Fe–Ni alloy, three layers, Fe_2O_3, $(Fe,Ni)_3O_4$, and $(Fe,Ni)O_x$ are subsequently formed on top of the Fe–Ni alloy substrate.[38] The Ni atoms in the Fe–Ni alloy can be bounded inside the $(Fe,Ni)_3O_4$ layer during the oxidation process and the top Fe_2O_3 layer is free of Ni. As a result, α-Fe_2O_3 NWs can be grown via the tip-growth mechanism. In addition, it has been mentioned that the tip-growth mechanism of NWs occurs via surface and internal diffusion. The surface diffusion has a lower energy barrier than internal diffusion, whereas the oxygen vacancies found at the α-Fe_2O_3 NWs can be considered to reduce the barrier height of internal diffusion, resulting in a decreased synthesis temperature for the growth of the NWs. In addition, it can be found that the density of oxygen deficiencies is decreased as the annealing temperature is increased. The formation of these oxygen deficiencies remains to be investigated in detail.[39]

2.4. Influence of Gas-Flow Rate

We now investigate the influence of gas-flow rate on the growth morphology. The gas-flow rate was changed from 70, to 100, to 150 sccm. The results show that the density of NWs is significantly increased and the NWs are uniformly distributed on the Fe-based alloy substrate on increasing the Ar gas flow rate; the NW density remains fairly uniform until the Ar gas flow rate is increased to 150 sccm. Such an example is shown in a series of SEM images in Figure 5a–c for the α-Fe_2O_3 NWs grown on an Fe film at 400 °C for 10 h with Ar flow rates of 70, 100, and 150 sccm, respectively. Figure 5d shows a magnified

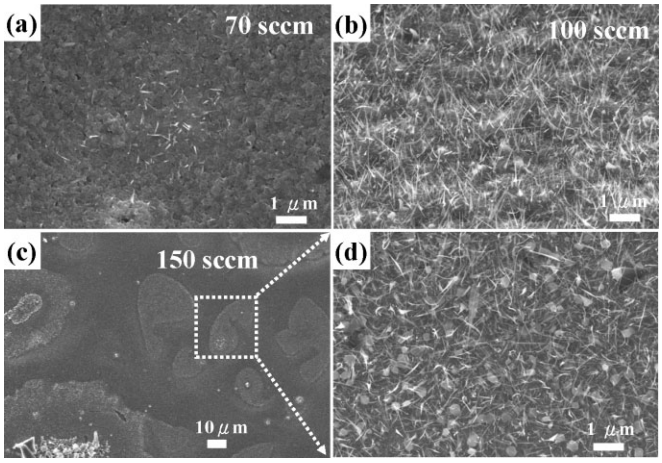

Figure 5. SEM images of α-Fe_2O_3 NWs grown on $Fe_{0.5}Ni_{0.5}$ at 400 °C for 10 h in Ar ambient at a flow rate of a) 70, b) 100, and c) 150 sccm. d) SEM image taken from the rectangular area in (c).

ADVANCED FUNCTIONAL MATERIALS

SEM image recorded from the rectangular area in Figure 5c. There are two possible factors that influence the NW growth: the oxygen concentration and resident time. If the concentration of oxygen vapor in the carrier gas is no more than the minimum value, the possibility for NW growth via the tip-growth mechanism is limited, resulting in few nanowires. Second, the different gas-flow rates also influence the resident time, τ, of the carrier gas during the growth of the NWs, which is a quantity defined to specify the interaction time of the gases with the growth substrates/products; thus, a simple equation is given[40]

$$\tau = \frac{P \times V}{Q} \quad (1)$$

where P, V, and Q represent the pressure and volume of the reaction chamber, and the flow rate, respectively. At a given pressure, the low flow rate can result in a long resident time that can easily cause different growth rates at different reaction areas, leading to the growth of non-uniformly distributed NWs on the alloy substrate. By reducing the resident time via increasing the flow rate, growth of uniformly distributed NWs can be enhanced. However, the density is nonuniform when the flow rate is more than 150 sccm because the oxygen vapor from decomposed α-Fe_2O_3 in the Ar carrier gas is oversaturated, resulting in different NW growth rates in different areas (Fig. 5c). Accordingly, the flow rate of 100 sccm found in the present study is a moderate value used to strike a balance between the oxygen-vapor concentration and resident time.

2.5. Influence of Growth Temperature

The next parameter to be examined is the growth temperature. Figure 6a–d show SEM images of α-Fe_2O_3 NWs grown on the $Fe_{0.5}Ni_{0.5}$ substrate with an Ar gas flux of 100 sccm at growth temperatures of 400, 500, 600, and 700 °C, respectively. Uniform, high-density α-Fe_2O_3 NWs with diameters of 10–40 nm and lengths up to several micrometers can be synthesized at a temperature of 400 °C. The diameter of these α-Fe_2O_3 NWs increases when the annealing temperature is increased. The increase of the annealing temperature can result in the enhancement of the diffusivity and reaction rate to elongate the NWs so that the density is decreased owing to Ostwald ripening.[41] At high annealing temperatures, the deviation in chemical potential between large and small materials becomes significantly important. If the dimension (size) of the nuclei in the initial growth of NWs is larger than the minimum size, they tend to coarsen. Otherwise, they tend to disappear, resulting in a decreased density of NWs during the growth period.

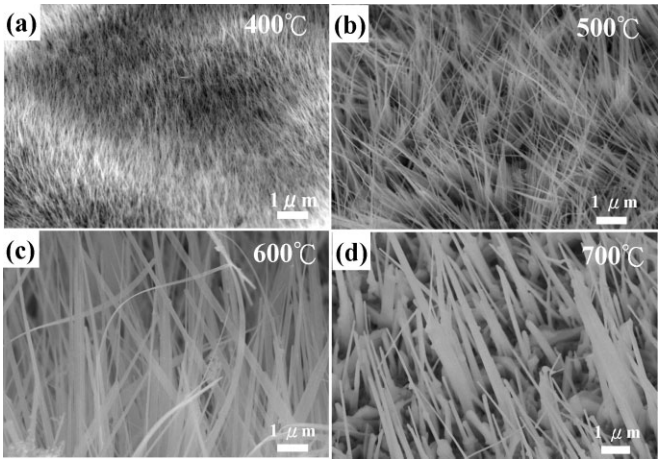

Figure 6. a–d) SEM images of α-Fe_2O_3 NWs grown on an $Fe_{0.5}Ni_{0.5}$ substrate at temperatures of 400, 500, 600, and 700 °C, respectively, using an Ar gas flux of 100 sccm.

2.6. Reducing Fe_2O_3 NWs to Fe_3O_4 NWs by a Reduction Process

We now examine the possibility of converting α-Fe_2O_3 NWs into Fe_3O_4 NWs by reduction. We started from the α-Fe_2O_3 NWs synthesized on an $Fe_{0.64}Ni_{0.36}$ substrate, and the reductive process was conducted in a mixed reductive ambient of H_2(5 %) + Ar(95 %) at different annealing temperatures. Figure 7a–c show the SEM images of the NWs after being annealed at 450, 500, and 600 °C, respectively, in a reductive ambient. For the sample reduced at an annealing temperature of 450 °C, few NWs were destroyed during the formation of the bulgelike shape, but most of the NWs did not experience much change in morphology. When the reductive temperature was increased to 500 °C, branched shapes could be found at the roots caused by fusing of the NWs during the reductive process, and the bulgelike morphology was also seen in many regions. When the reductive temperature was increased to 600 °C, most of the NWs formed branch- and bulgelike features and the density was significantly decreased as a result of fusing and bunching.

Figure 7d shows the TEM image of an α-Fe_2O_3 NW sample annealed at 450 °C in a reductive ambient. The diameters of these NWs are about 10–80 nm and the corresponding diffraction pattern in the inset of Figure 7d obviously confirms that the phase of these NWs is Fe_3O_4. The upper inset in Figure 7e shows a low-magnification TEM image of an Fe_3O_4 NW with a taperlike feature, indicating that the NW keeps the original shape after reduction. The diffraction pattern, as shown in the bottom inset in Figure 7e, confirms and reveals the single-crystal nature with the [111] zone axis. Two spacings of 0.29 nm are consistent with the planes of $(02\bar{2})$ and $(20\bar{2})$, and the NW growth direction is $[1\bar{1}0]$.

Figure 7f shows the EELS spectrum of oxygen K-edge and Fe L-edge ELNES for the α-Fe_2O_3 NW before and after the reduction process. No chemical shift in the L_3 line or change in the separation between L_3 and L_2 can be found but the intensity ratio I(L3)/I(L2) decreased from 4.2 for α-Fe_2O_3 NWs to 3.9 for Fe_3O_4 NWs. In addition, the intensity of peak c in the oxygen K-edge ELNES spectrum of the α-Fe_2O_3 NW after the reduction process is evidently increased, also confirming the Fe_3O_4 phase.[26] Though a similar spectrum can be found in γ-Fe_2O_3 NWs, the analysis of the diffraction pattern and EELS spectrum can allow us to confidently conclude that the phase of the NWs after the reduction process is Fe_3O_4.[33]

Figure 7g shows the TEM image of an Fe_3O_4 nanowire taken from the α-Fe_2O_3 NW sample after annealing at 600 °C. It is

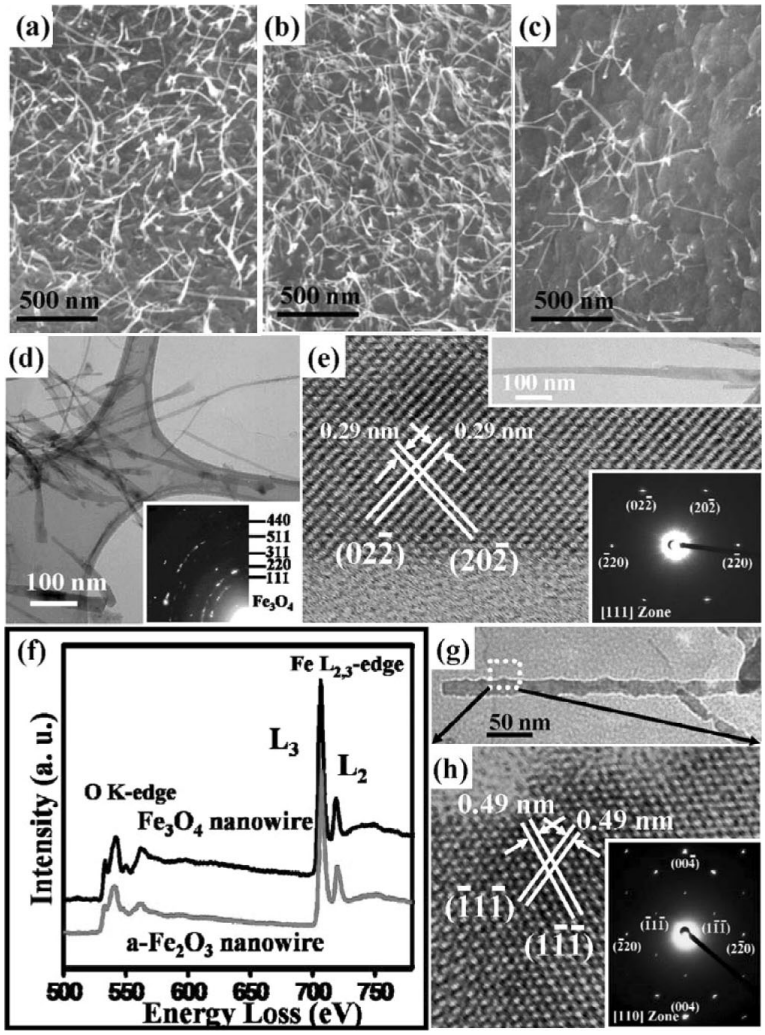

Figure 7. SEM images of Fe_3O_4 NWs synthesized by converting α-Fe_2O_3 NWs in a reductive ambient for 20 min at a) 450, b) 500, and c) 600 °C. The α-Fe_2O_3 NWs were grown on an $Fe_{0.64}Ni_{0.36}$ alloy substrate at 400 °C for 10 h in a Ar ambient. d) TEM image of the converted NWs. The inset shows the corresponding diffraction pattern. e) High-resolution TEM image of the Fe_3O_4 NWs. The upper inset shows the low-magnification TEM image. The bottom inset shows the corresponding diffraction pattern with [111] zone axis. f) The EELS spectrum of the oxygen K-edge ELNES and Fe L-edge for both the α-Fe_2O_3 and Fe_3O_4 NWs, respectively. g) TEM image of Fe_3O_4 NWs converted from α-Fe_2O_3 NWs at 600 °C in a reductive ambient. h) The corresponding high-resolution TEM image recorded from the rectangular area shown in (g). The inset shows the diffraction pattern with [110] zone axis.

clear that the surface is very rough. Furthermore, the high-resolution TEM image obtained from the rectangular area in Figure 7g is shown in Figure 7h, confirming the single-crystal nature with a growth direction of [1$\bar{1}$0], where the corresponding diffraction pattern with the [110] zone axis is presented.

2.7. In Situ Phase Transformation from α-Fe_2O_3 NWs to Fe_3O_4 NWs

In order to give more evidence of the synthesis of Fe_3O_4 NWs by simply annealing the α-Fe_2O_3 NWs in a reductive ambient, direct observation of phase and structure transformation from α-Fe_2O_3 to Fe_3O_4 was conducted by in situ TEM. Though it is hard to maintain the reductive ambient in the TEM chamber, the annealing of α-Fe_2O_3 NWs in the vacuum chamber can be considered another kind of reductive reaction.[42] An α-Fe_2O_3 NW was dispersed on a Mo grid with one end of the NW fastened and the other suspended, as shown in Figure 8a. The dark line in the α-Fe_2O_3 NW is suggested to be a defect and could be used as a reference point during in situ annealing. It is found that the morphology of the NWs remains unchanged when the annealing temperature is increased to 500 °C, and starts to change when the annealing temperature is increased to 700 °C. Furthermore, the surface becomes much rougher but still maintains the original shape when the annealing temperature is increased to 900 °C. The corresponding high-resolution TEM image taken from the rectangular area in Figure 8e is shown in Figure 8f. The diffraction pattern, as shown in the inset of Figure 8f, confirms the Fe_3O_4 phase with a [110] zone axis. Two spacings of 0.48 nm are found, which are consistent with the ($\bar{1}1\bar{1}$) and (1$\bar{1}\bar{1}$) planes. From the diffraction pattern and high-resolution TEM image, the NW growth direction was found to be [1$\bar{1}$0], which is perpendicular to the (111) close-packed plane. O atoms inside the α-Fe_2O_3 and Fe_3O_4 were found to have ABAB... and ABCABC... stackings, respectively. The corresponding hard-ball models are illustrated in Figure 8g and h. Accordingly, the oxygen vacancies found in α-Fe_2O_3 NWs may play an important role in the mediation of the structure transformation, resulting in the remaining original morphology where the growth direction of the NWs was converted from [110] for α-Fe_2O_3 NWs to [1$\bar{1}$0] for Fe_3O_4 NWs.

2.8. Characterization

2.8.1. Magnetic Properties

We now examine the properties of the magnetic NWs. Figure 9a–d provides the results of magnetic measurements on the α-Fe_2O_3 and Fe_3O_4 NWs. For the measurements, all of the NWs were dispersed on a Si substrate in order to avoid the magnetic signal from the Fe-based alloy substrate interfering with the magnetic measurements. Figure 9a shows the hysteresis loops of the NWs measured by vibrating sample magnetometry measurements by applying the magnetic field parallel and perpendicular to the Si substrate. The hysteresis loop indicates very weak ferromagnetism as the applied magnetic field is applied parallel to the Si substrate (parallel to the α-Fe_2O_3 NWs), while it indicates diamagnetism as the magnetic field is applied perpendicular to the Si substrate (perpendicular to the α-Fe_2O_3 NWs). The corresponding SEM image was taken after applying the magnetic field along

ADVANCED FUNCTIONAL MATERIALS

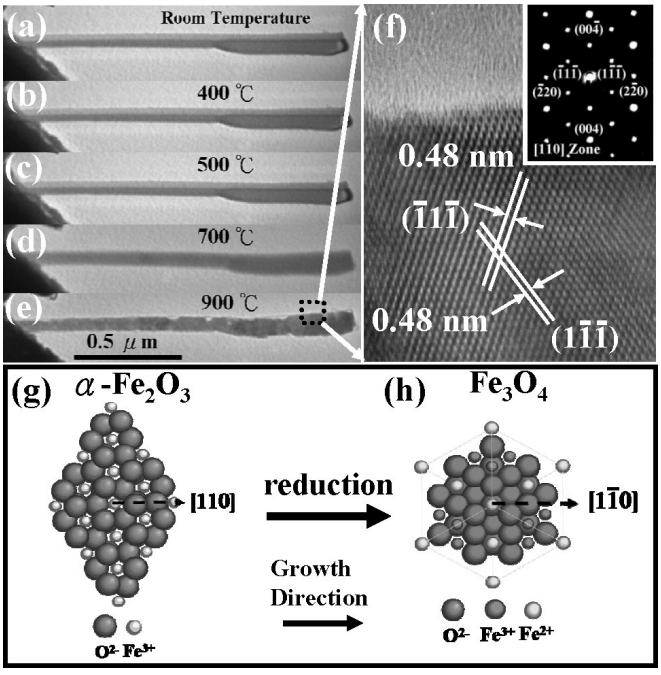

Figure 8. a–e) TEM images of phase and structure transformation from α-Fe_2O_3 to Fe_3O_4 NWs at different annealing temperatures. f) A high-resolution TEM image taken from the rectangular area in (e). The corresponding diffraction pattern confirms the Fe_3O_4 phase with [110] zone axis. g,h) Atomic model of transformation of α-Fe_2O_3 (with oxygen vacancies) to Fe_3O_4.

the direction of the arrow that is parallel to the Si substrate as shown in Figure 9b. The inset in Figure 9b shows the magnified SEM image taken from the rectangular area shown in Figure 9b. It is obvious that all of the α-Fe_2O_3 NWs are still randomly distributed after applying the magnetic field. α-Fe_2O_3 is an antiferromagnetic material and the two antiferromagnetic spins are along the [001] direction below the Morin temperature ($T_M = 260$ K). When the temperature is between 260 and 955 K (Ne'el temperature), α-Fe_2O_3 can exhibit weak ferromagnetic behavior, which is called parasitic ferromagnetism.[43] However, oxygen vacancies inside the α-Fe_2O_3 NWs may destroy the balance of antiferromagnetic behavior, resulting in the extremely weak ferromagnetism. Accordingly, the force generated by the external field is insufficient to rearrange the NW parallel to the applied field due to the extremely weak interaction between the external magnetic field and the α-Fe_2O_3 NWs. On the other hand, it can be considered that the magnetic signal from the α-Fe_2O_3 NWs is much smaller than that from the Si substrate when the applied magnetic field is perpendicular to the Si substrate (perpendicular to the NWs), resulting in the diamagnetic feature in the hysteresis loop originating from the Si substrate (the magnetic susceptibility $X_m = -5.2 \times 10^{-6}$).[44]

Figure 9c shows the hysteresis loop of Fe_3O_4 NWs dispersed on the Si substrate obtained by applying the magnetic field parallel and perpendicular to the Si substrate. Ferromagnetic behavior is exhibited by the hysteresis loops for both applied directions (perpendicular and parallel to the Si substrate). A high remanent (residual magnetization) with a coercive field of about 220 Oe (1 Oe = 1000/4π A m^{-1}) can be found, which is consistent with previous reports when the applied magnetic field is parallel to the substrate. The remanent decreases when the applied magnetic field is perpendicular to the Si substrate, with a coercive field of 140 Oe.[7,45–47] The high remanent and coercive fields may result from the shape anisotropy, forcing the magnetic moments to mostly align along the axis of the NWs. The larger data variation was found at both the hysteresis loops (magnetization–magnetic field (*M–H*) curves), which may be caused by the movement of the NWs during measurement. Figure 9d shows the SEM image of Fe_3O_4 NWs after applying the magnetic field parallel to the Si substrate. All of the NWs are aligned along one direction after applying the magnetic field parallel to the substrate.

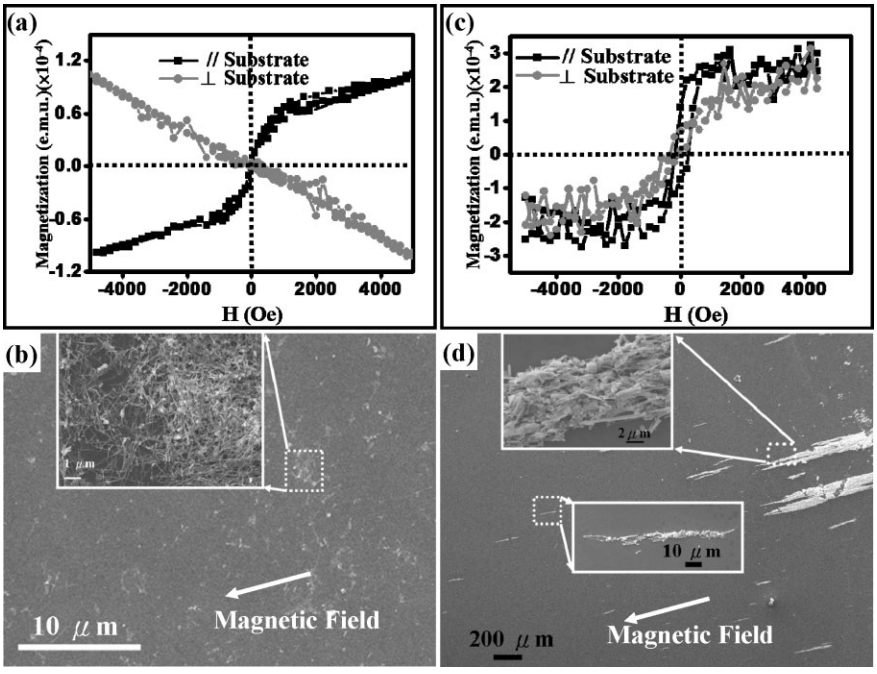

Figure 9. a) Hysteresis loops of α-Fe_2O_3 NWs measured by vibrating sample magnetometry with the magnetic field applied perpendicular and parallel to the substrate. b) SEM image of α-Fe_2O_3 NWs dispersed on Si substrate after applying the magnetic field parallel to the substrate. c) Hysteresis loop of the Fe_3O_4 NWs measured by vibrating sample magnetometry with the magnetic field applied perpendicular and parallel to the substrate. d) SEM image of Fe_3O_4 NWs dispersed on Si substrate after applying the magnetic field. Insets in (b) and (d) show the magnified SEM images recorded from the corresponding rectangular areas.

2.8.2. Field-Emission Properties of α-Fe_2O_3 NWs

The high density of α-Fe_2O_3 NWs has the potential for use in field-emission devices. The corresponding current density (*J*) as a function of the applied electric

field (E) with a separation of 100 μm between the anode and emitting surface is shown in Figure 10. The measurement was carried out several times. The turn-on and threshold fields are defined as the fields required for achieving current densities of

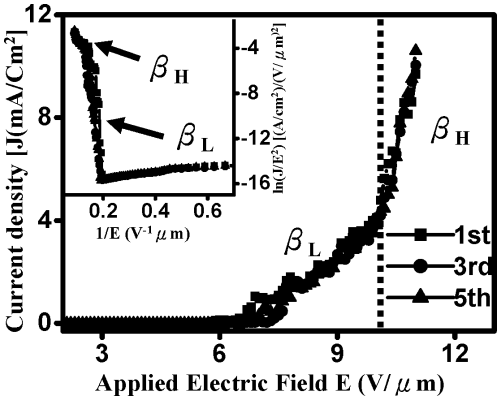

Figure 10. J as a function of E. Two slopes can be unambiguously found. The inset shows a plot of $\ln(J/E^2)$ against $1/E$.

0.01 and 10 mA cm^{-2}, respectively. The turn-on and threshold fields were measured to be about 6.3 and 10 V μm^{-1}, respectively. The Fowler–Nordheim (F–N) plot of $\ln(J/E^2)$ against $1/E$ is shown in the inset of Figure 10. The straight line indicates that the field-emission behavior follows the F–N mechanism where the electrons can tunnel through the potential barrier from conduction band to a vacuum state. The F–N relationship can be simply expressed by Equation 2[48]

$$J = (A\beta^2E^2 / \Phi) \exp(-B\Phi^{3/2} / \beta E) \quad (2)$$

where Φ is the work function; A and B are constants corresponding to 1.56×10^{-10} $AV^{-2}eV$ and 6.83×10^3 $VeV^{-3/2}\mu m^{-1}$, respectively; β is the field-enhancement factor, which is used to indicate the degree of the field-emission enhancement of any tip shape on a planar surface; and β is a parameter depending on the geometry of the NW, crystal structure, and the density of the emitting points. It is worth pointing out that two slopes are found at the low- and high-field regions in the J–E and F–N plots. Accordingly, the field enhancement at low and high electric fields, β_L and β_H, can be determined to be about 560 and 1500 by calculating the slopes of $\ln(J/E^2) - (1/E)$ with the work function of 5.6 eV.[49] These two slopes found in the J–E and F–N plots can be attributed to the semiconductor feature of NWs where the electrons emitted from the NWs may originate from two successive processes: the excitation of electrons from the valance to the conduction band, and the emission from the conduction band to the vacuum. At low applied voltages, a few electrons can be excited from the valance band to the conduction band and emitted from the NWs. When the applied voltage is increased to a critical value, all of the electrons can be totally excited from the valence band to the conduction band, exhibiting the quasimetallic behavior that can result in the increased β value in the high-field region. Compared to the β values of other materials, such as Si nanowires ($\beta = 1000$),[50] $NiSi_2$ nanorods ($\beta = 630$),[51] $TiSi_2$ nanowires ($\beta = 501$),[52] SnO_2 ($\beta = 1402.9$),[53] and AlN ($\beta = 950$),[54] the low turn-on field and high β value for the NWs here exhibit their promising potential in field emission.

3. Summary

In this paper, we have systematically investigated the experimental conditions, such as type of substrate, local growth and geometrical environment, gas-flow rate and growth temperature, under which high-density α-Fe_2O_3 NW arrays can be grown by a solid-phase route via the tip-growth mechanism. The synthesized temperature can be as low at 400 °C. By increasing the concentration of Ni in the Fe-based alloy substrate, the density of the α-Fe_2O_3 NWs can be significantly increased due to the fact that the Ni atoms in the Fe-based alloy can enhance the diffusion coefficient of Fe. By placing the substrate perpendicular to the alumina stage, different nanostructure morphologies are obtained, indicating that the local turbulence and/or vapor pressure is critical for the formation of the NWs. In addition, the gas-flow rate and synthesis temperature are investigated. From the TEM analysis, the growth direction of α-Fe_2O_3 NWs is [110], and the ordered oxygen vacancies are found in the α-Fe_2O_3 NWs. EELS analysis indicates that the oxidation states of the Fe cations are partially reduced from Fe^{3+} to Fe^{2+} in order to balance the charge created by the oxygen vacancies.

The conversion of α-Fe_2O_3 NWs into Fe_3O_4 NWs has been carried out by simply annealing the α-Fe_2O_3 NWs in a reductive ambient at a high temperature. The growth direction of the converted NWs is $[1\bar{1}0]$, which is perpendicular to the close-packed plane of (111). It is suggested that the oxygen vacancies presented in α-Fe_2O_3 NWs play a significant role in transforming the structure. The magnetic and field-emission properties of the α-Fe_2O_3 NWs during their transition into Fe_3O_4 NWs have been investigated.

4. Experimental

Four types of iron-based substrates were used, including Fe–Ni alloy plates with a composition of 1:1 and 64:36 (atomic percentage), bulk iron (purity > 99.995 %), and iron film deposited on a Si wafer using a non-ultrahigh-vacuum electron-beam system with a thickness of 1 μm. All of the substrates were cut into small pieces of 1.5 cm^2 and ultrasonically cleaned using alcohol (99.95 %). The furnace used in the present study is a typical three-zone tube furnace, including a vacuum pumping system, an alumina tube, a quartz tube, and a gas-flow system that was produced by Zimberger Inc. The ultimate vacuum level for this configuration is 3×10^{-2} Torr (1 Torr ≈ 133 Pa) and the maximum output temperature can reach ca. 1500 °C. A schematic diagram of the experiment is shown in Figure 11. The quartz tube was set into the alumina tube in order to avoid contamination of the external alumina tube during synthesis of the NWs. The system was pumped to a base pressure of 3×10^{-2} Torr and then maintained at the pressure of 500–1000 mbar (1 mbar = 100 Pa) by introducing Ar carrier gas (99.995 %) at a flow rate of 70–150 sccm, which was controlled by the maximum flow controller (MFC). It is worth pointing out that all of the samples needed to

ADVANCED FUNCTIONAL MATERIALS

be tilted by 90° on an Al_2O_3 stage and put into the lower-temperature region of 350–700 °C for 10 h. 5 g of α-Fe_2O_3 commercial powder was placed in the high-temperature region of 1200 °C. A constant ramping rate of 5 °C min^{-1} was used to raise the temperature to a desired value and the system was allowed to cool down naturally to room temperature.

During the conversion of the nanowires, the reduction procedure was carried out in a mixed reductive ambient of H_2(5 %) + Ar(95 %) using the as-prepared α-Fe_2O_3 NWs annealed at a temperature of 400–600 °C for 20 min in the furnace.

The surface morphology was examined by a field-emission scanning electron microscope (JSM-6500F), operated at 15 kV. In order to prepare the TEM specimen, all samples were sonicated in ethanol and then dispersed on a copper grid supported by a holey carbon film. A field-emission transmission electron microscope (JEM-3000F) operated at 300 kV with a point-to-point resolution of 0.17 nm equipped with an energy dispersion spectrometer (EDS) and an electron energy loss spectrometer were used to characterize the microstructures and chemical compositions. The magnetic properties were characterized by vibrating sample magnetometry. The electron field-emission behavior was measured in a vacuum of 1×10^{-7} Torr using a spherical stainless-steel probe (1 mm in diameter) as the anode. The lowest emission current was recorded on the level of nanoamps. The measurement distance between the anode and the emitting surface was fixed at 100 μm.

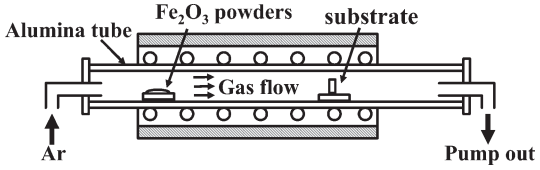

Figure 11. The configuration of furnace for the synthesis of Fe_2O_3 NWs.

Received: June 7, 2006
Revised: June 28, 2006
Published online: October 2, 2006

[1] C. S. Lao, P. X. Gao, L. Zhang, D. Davidovic, R. Tummala, Z. L. Wang, *Nano Lett.* **2006**, *6*, 263.
[2] J. Zhou, S. Z. Deng, L. Gong, Y. Ding, J. Chen, J. X. Huang, J. Chen, N. S. Xu, Z. L. Wang, *J. Phys. Chem. B* **2006**, *110*, 10 296.
[3] A. Ponzoni, E. Comini, G. Sberveglieri, J. Zhou, S. Z. Deng, N. S. Xu, Y. Ding, Z. L. Wang, *Appl. Phys. Lett*. **2006**, *88*, 203 106.
[4] Y. Zhang, L. Li, H. Li, L. D. Zhang, *Phys. Rev. B* **2006**, *73*, 113 403.
[5] B. Y. Geng, X. W. Liu, Q. B. Du, X. W. Wei, L. D. Zhang, *Appl. Phys. Lett*. **2006**, *88*, 163 104.
[6] S. Yang, H. Zhu, D. Yu, Z. Jin, S. Tang, Y. Ru, *J. Magn. Magn. Mater.* **2000**, *222*, 97.
[7] D. H. Zhang, Z. Q. Liu, S. Hau, C. Li, B. Lei, M. D. Stewart, J. M. Tour, C. W. Zhou, *Nano Lett.* **2004**, *4*, 2151.
[8] P. Chauhan, S. Annapoorni, S. K. Trikha, *Thin Solid Films* **1999**, *346*, 266.
[9] T. Ohmori, H. Takahashi, H. Mametsuka, E. Suzuki, *Phys. Chem. Chem. Phys.* **2000**, *2*, 3519.
[10] W. Weiss, D. Zscherpel, R. Schlogl, *Catal. Lett.* **1998**, *52*, 215.
[11] Y. Fu, J. Chen, H. Zhang, *Chem. Phys. Lett.* **2001**, *350*, 491.
[12] R. M. Cornell, U. Schwertmann, *The Iron Oxide: Structure, Properties, Reactions, Occurrence, and Uses*, VCH, New York **1996**.
[13] Y. Fu, J. Chen, H. Zhang, *Chem. Phys. Lett.* **2003**, *379*, 373.
[14] X. G. Wen, S. H. Wang, Y. Ding, Z. L. Wang, S. Yang, *J. Phys. Chem. B* **2005**, *109*, 215.
[15] J. Wang, Q. W. Chen, C. Zheng, B. Y. Hou, *Adv. Mater.* **2004**, *16*, 137.
[16] J. X. Wan, X. Y. Chen, Z. H. Wang, X. G. Yang, Y. T. Qian, *J. Cryst. Growth* **2005**, *276*, 371.
[17] D. S. Xue, L. Y. Zhang, C. X. Gao, X. F. Xu, A. B. Gui, *Chin. Phys. Lett.* **2004**, *21*, 773.
[18] J. B. Yang, H. Xu, S. X. You, X. D. Zhou, C. S. Wang, W. B. Yelon, W. J. James, *J. Appl. Phys.* **2006**, *99*, 08Q507.
[19] F. Liu, P. J. Cao, H. U. Zhang, J. F. Tian, C. W. Xiao, C. M. Shen, J. Q. Li, H. J. Gao, *Adv. Mater.* **2005**, *17*, 1893.
[20] C. H. Ye, X. S. Fang, Y. F. Hao, X. M. Teng, L. D. Zhang, *J. Phys. Chem. B* **2005**, *109*, 19 758.
[21] Y. F. Hao, G. W. Meng, C. H. Ye, X. R. Zhang, L. D. Zhang, *J. Phys. Chem. B* **2005**, *109*, 11 204.
[22] Y. F. Hao, G. W. Meng, C. H. Ye, L. D. Zhang, *Cryst. Growth Des.* **2005**, *5*, 1617.
[23] E. I. Givargizov, *Highly Anisotropic Crystal*, 8th ed., Terra Scientific, Tokyo **1987**.
[24] R. Takagi, *J. Phys. Soc. Jpn.* **1957**, *12*, 1212.
[25] B. Million, J. Ruzickova, J. Velisek, J. Verstal, *Mater. Sci. Eng.* **1981**, *50*, 43.
[26] I. N. Franstevich, D. F. Kalinovich, I. I. Kovenskii, M. D. Smolin, *J. Phys. Chem. Solids* **1969**, *30*, 947.
[27] T. Ustad, H. Sorum, *Phys. Status Solidi* **1973**, *20*, 286.
[28] B. Y. Zong, Y. H. Wu, G. H. Han, B. J. Yang, P. Luo, L. Wang, J. J. Oiu, K. B. Li, *Chem. Mater.* **2005**, *17*, 1515.
[29] G. Y. Yang, E. C. Dickey, C. A. Randall, M. S. Randall, L. A. Mann, *J. Appl. Phys.* **2003**, *94*, 5990.
[30] A. Travlos, N. Boukos, G. Apostolopoulos, A. Dimoulas, *Appl. Phys. Lett.* **2003**, *82*, 4053.
[31] Z. L. Wang, J. S. Yin, Y. D. Jiang, J. Zhang, *Appl. Phys. Lett.* **1997**, *70*, 3362.
[32] C. Colliex, M. Tencé, E. Lefèvre, C. Mory, H. Gu, D. Bouchet, C. Jeanguillaume, *Mikrochim. Acta* **1994**, *114*, 71.
[33] C. Colliex, T. Manoubi, C. Ortiz, *Phys. Rev. B* **1991**, *44*, 11 402.
[34] H. Kurata, E. Lefèvre, C. Colliex, R. Brydson, *Phys. Rev. B* **1993**, *47*, 13 763.
[35] J. Jasinski, K. E. Pinkerton, I. M. Kennedy, V. J. Leppert, *Sens. Actuators B* **2005**, *109*, 19.
[36] D. H. Pearson, B. Fultz, C. C. Ahn, *Appl. Phys. Lett.* **1988**, *53*, 1405.
[37] Z. L. Wang, J. S. Yin, *Philos. Mag. B* **1998**, *77*, 49.
[38] J. H. Zhu, Office of Fossil Energy Fuel cell program, FY **2005** annual report, III. A.16 P113, Tampa, FL.
[39] J. Q. Liang, M. T. Chang, Y. L. Chueh, L. J. Chou, unpublished.
[40] A. Grill, *Cold Plasma in Materials Fabrication: From Fundamentals to Application*, IEEE, New York **1993**.
[41] M. Ohring, *The Materials Science Of Thin Films*, Academic, San Diego, CA **1992**.
[42] Z. L. Wang, J. S. Yin, W. D. Mo, Z. J. Zhang, *J. Phys. Chem. B* **1997**, *101*, 6793.
[43] M. F. Hansen, C. B. Koch, S. Morup, *Phys. Rev. B* **2000**, *62*, 112 432.
[44] S. O. Kasap, *Principle Of Electronic Materials and Devcies*, 2nd ed., McGraw Hill, New York **2002**.
[45] L. Q. Xu, W. Q. Zhang, Y. W. Ding, Y. Y. Deng, S. Y. Zhang, W. C. Yu, Y. F. Qian, *J. Phys. Chem. B* **2004**, *108*, 10 859.
[46] J. Wang, Q. W. Chen, C. Zeng, B. Y. Hou, *Adv. Mater.* **2004**, *16*, 137.
[47] W. Shi, H. Zeng, Y. Sahoo, T. Y. Ohulchanskyy, Y. Ding, Z. L. Wang, M. Swihart, P. N. Prasad, *Nano Lett.* **2006**, *6*, 875.
[48] Y. L. Chueh, L. J. Chou, C. H. Hsu, S. C. Kung, *J. Phys. Chem. B* **2005**, *109*, 21 831.
[49] E. R. Batista, R. A. Friesner, *J. Phys. Chem. B* **2002**, *106*, 8136.
[50] Y. L. Chueh, L. J. Chou, S. L. Cheng, J. H. He, W. W. Wu, L. J. Chen, *Appl. Phys. Lett.* **2005**, *86*, 133 112.
[51] Y. W. Ok, T. Y. Seong, C. J. Choi, K. N. Tu, *Appl. Phys. Lett.* **2006**, *88*, 043 106.
[52] Q. Xiang, Q. X. Wang, Z. Wang, X. Z. Zhang, L. Q. Liu, J. Xu, D. P. Yu, *Appl. Phys. Lett.* **2005**, *86*, 243 103.
[53] J. H. He, T. H. Wu, C. L. Hsin, K. M. Li, L. J. Chen, Y. L. Chueh, L. J. Chou, Z. L. Wang, *Small* **2006**, *2*, 116
[54] J. H. He, R. S.Yang, Y. L. Chueh, L. J. Chou, L. J. Chen, Z. L.Wang, *Adv. Mater.* **2006**, *18*, 650.